RSC Advances

PAPER

View Article Online
View Journal | View Issue

Check for updates

Cite this: *RSC Adv.*, 2017, 7, 55020

A magnetic $CoFe_2O_4$–CNS nanocomposite as an efficient, recyclable catalyst for peroxymonosulfate activation and pollutant degradation†

Chang-Bin Chen,*[ab] Feng Zhang,*[a] Chen-Xuan Li,[ab] Jia-Yuan Lu,[a] Shuo Cui,[ab] Hou-Qi Liu[ab] and Wen-Wei Li *[ab]

Received 31st August 2017
Accepted 27th November 2017

DOI: 10.1039/c7ra09665h

rsc.li/rsc-advances

Sulfate radical ($SO_4^{\bullet-}$) based advanced oxidation processes allow efficient degradation of refractory organics, but efficient, low-cost, and robust catalysts for such processes are still lacking. In this work, a magnetically recoverable heterogeneous catalyst was fabricated by immobilizing spinel cobalt-ferrite ($CoFe_2O_4$) particles on graphitic carbon nitride nanosheets (CNS) using a low-cost, one-step solvothermal method. In the $CoFe_2O_4$–CNS nanocomposite, the $CoFe_2O_4$ particles were evenly-distributed on the CNS surface, giving the nanocomposite a high specific surface area and significantly raised activity for peroxymonosulfate (PMS) activation and sulfonamide degradation compared to the bare $CoFe_2O_4$ NPs, which were considerably aggregated. In addition, the $CoFe_2O_4$–CNS could be more efficiently separated under magnetic field and resuspended compared with the bare $CoFe_2O_4$ due its larger sizes and no agglomeration. A stable activity of the nanocomposite catalyst during repeated use was also demonstrated. Our results imply high potential of $CoFe_2O_4$–CNS for sustainable water treatment and environmental remediation applications.

1. Introduction

Advanced oxidation processes (AOP) based on the sulfate radical ($SO_4^{\bullet-}$) are promising alternatives to those based on hydroxyl radicals for water treatment and environmental remediation applications, with advantages such as high redox potential (2.5–3.1 V),[1] relatively long lifetime and wide pH range.[2] $SO_4^{\bullet-}$ can be efficiently generated from peroxymonosulfate (PMS)[3] or persulfate (PS)[4,5] by using transition metals as catalysts. Cobalt (Co)-based materials are the most efficient catalysts for PMS activation so far.[6,7] In particular, heterogeneous Co catalysts are gaining growing interest because they can be reused and are environmentally-benign.[8–10] To facilitate their recovery after use, spinel-type Co-bearing ferrite nanoparticles ($CoFe_2O_4$ NPs) have been recently developed, which show high catalytic activity and good adaptability to magnetic separation.[11] However, such nanoparticles are difficult to magnetically separate from the water phase due to their small sizes.[12,13] Another challenge is the easy agglomeration of the NPs, which leads to poor re-suspension and reduced performance with repeated use.[11] One strategy to address the NPs separation and agglomeration issue is to disperse the NPs on various support materials, including reduced graphene oxide (rGO),[14] carbon nanotube,[15] titanate nanotubes.[16,17] Recently, the combination of $CoFe_2O_4$ with graphitic carbon nitride ($g\text{-}C_3N_4$, a low-cost, highly-stable, and porous 2D materials with unique photocatalytic activity[18–21]) has also been proposed. The $CoFe_2O_4/g\text{-}C_3N_4$ showed high photocatalytic activity for degradation Rhodamine B,[22,23] but has not been used for $SO_4^{\bullet-}$-based AOP so far. In addition, the synthesis process of the composite (involving precipitation, ultrasonic mixing and calcining) is complicated, and bulk $g\text{-}C_3N_4$ (ref. 22 and 23) with large size and low specific surface area was typically used.[24,25]

Inspired by the above studies, here we investigated the feasibility of using $CoFe_2O_4/g\text{-}C_3N_4$ as a catalyst for activation of PMS. To improve its catalysis and recovery performances, we adopted a simple, one-step solvothermal method for the material fabrication, and used ultrathin $g\text{-}C_3N_4$ nanosheet (CNS) as the support for $CoFe_2O_4$.[18] The catalytic activities of the resulting $CoFe_2O_4$–CNS nanocomposite and the $CoFe_2O_4/g\text{-}C_3N_4$ obtained by conventional method were evaluated by using sulfonamide (SA) as a model pollutant. SA is a ubiquitous, persistent contaminant, with high risks to aquatic ecosystem and human health.[26–30] In addition, SA is a rich-electronic compound, which is suitable for $SO_4^{\bullet-}$-based AOP.[3,31,32] The magnetic separation and re-suspension performances and the stability of the materials during repeated use were also investigated. Lastly, the catalytic mechanisms of the nanocomposite for PMS activation were elucidated.

---

[a] *CAS Key Laboratory of Urban Pollutant Conversion, Department of Chemistry, University of Science & Technology of China, Hefei, 230026, China*

[b] *Collaborative Innovation Center of Suzhou Nano Science and Technology, Suzhou, 215123, China*

† Electronic supplementary information (ESI) available. See DOI: 10.1039/c7ra09665h

2. Experimental

2.1. Materials

Iron chloride ($FeCl_3 \cdot 6H_2O$), cobalt dichloride ($CoCl_2 \cdot 6H_2O$), sodium acetate (NaAc), and ethylene glycol, ethanol, melamine, sulfanilamide, methanol, *tert*-butyl alcohol (TBA), all of analytical grade, were purchased from Sinapharm Chemical Reagent Co., Ltd. Peroxymonosulfate (PMS, Oxone) was purchased from J&K Scientific LTD. All the solutions were prepared with deionized (DI) water.

2.2. Synthesis of $CoFe_2O_4$–CNS catalyst

The CNS were synthesized according to the method described in a previous report.[21] Melamine (5 g) was calcined at 520 °C for 4 h with the heating rate of 5 °C min^{-1} to obtain yellow bulk g-C_3N_4. Then, the bulk g-C_3N_4 was milled into powder, transferred into a combustion boat without any cover, and heated at 550 °C for 3 h to obtain CNS. The resulting CNS (200 mg) was added into 30 mL ethylene glycol solution under ultrasonication, followed by adding 2 mmol $FeCl_3 \cdot 6H_2O$ and 1 mmol $CoCl_2 \cdot 6H_2O$. Then, 15 mmol sodium acetate, as a protective agent to control the shape of synthesized nanomaterials, was added into the solution under vigorous stirring at room temperature. The mixture was subsequently autoclaved in a 50 mL Teflon lined stainless steel autoclave at 180 °C for 24 h, and then naturally cooled down to room temperature. The resulting black precipitate was collected by filtration and washed with absolute ethanol and DI water in sequence for several times. The final product was dried in a vacuum box at 60 °C for 6 h prior to use. For comparison, the bare $CoFe_2O_4$ was fabricated without the addition of g-C_3N_4 following the same procedures.[33,34] In addition, graphene oxide-supported $CoFe_2O_4$ ($CoFe_2O_4$–GO) was prepared following a reported method.[35]

2.3. Catalytic activity test

The catalytic activities of different materials for PMS activation and SA degradation was examined. The bare $CoFe_2O_4$ NPs and g-C_3N_4 were used as the controls. Before the degradation test, SA was added into 100 mL DI water under constant stirring to an initial concentration of 10 mg L^{-1}. Then, 100 mg L^{-1} catalyst and 100 mg L^{-1} PMS were added to initiate the degradation reactions. During the test, 1 mL mixed liquor was collected each time at given time intervals, immediately quenched with excess pure methanol (1 mL), and then centrifuged before analysis. All the experiment was conducted in duplicate at ambient temperature (25 ± 2 °C).

2.4. Analysis

The SA concentration was measured by a liquid chromatograph (Alliance, water 2695) equipped with Waters 2487 dual λ absorbance detector and Agilent 5 TC-C18 150 × 4.6 mm column. A mixture of methanol and 0.1% formic acid solution (20 : 80, v/v) at a flow rate of 0.5 mL min^{-1} was used as the mobile phase. The column temperature was 30 °C. The detection wavelength was set at 268 nm.

The morphology and structure of the materials were examined by scanning electron microscopy (SEM, QUSNTA FEG 250) and transmission electronic microscopy (TEM, HT7700). X-ray diffraction (XRD) patterns were obtained on a Bruker D8 diffractometer using filtered Cu Kα radiation ($\alpha = 1.54178$ Å). The Brunauer–Emmett–Teller (BET) specific surface area of sample was determined on an Autosorb iQ Station 3 system at liquid-nitrogen temperature of 77.35 K. The chemical species of Co, Fe, O, C and N were determined by X-ray photoelectron spectroscopy (XPS). Magnetic properties of the samples were examined using a MPMS (SQUID)-vibrating sample magnetometer at 300 K.

3. Results

3.1. Catalysts characterization

The morphologies of the CNS, bare $CoFe_2O_4$ and $CoFe_2O_4$–CNS composite are shown in Fig. 1. The CNS had large sizes ranging from hundreds of nanometer to several micrometer (Fig. 1(a)) but a small thickness of around 10 nm (Fig. 1(d)). The bare $CoFe_2O_4$ was mainly in the shape of spherical particles that aggregated together (Fig. 1(b) and (e)). In comparison, for the $CoFe_2O_4$–CNS composites, the particles were evenly distributed on the CNS (Fig. 1(c) and (f)). The particles did not peel off from the CNS after ultrasonic processing for 30 min due to the formation of heterostructured material. The high resolution TEM (HRTEM) image of $CoFe_2O_4$–CNS showed lattice fringe spacing of 0.24 nm, 0.25 nm, 0.29 nm and 0.487 nm (Fig. 1(g) and (h)), consistent with the (2 2 2) (3 1 1) (2 2 0) and (1 1 1) planes of $CoFe_2O_4$ crystals, respectively.[36,37] No clear lattice was observed for the CNS due to its low crystallinity. The two components were tightly bonded together, as indicated by the clear interface between them. In addition, the EDX spectra confirm the presence of Co, Fe, C, O, and N elements in the $CoFe_2O_4$–CNS (Fig. 1(i)). The Si signal observed here was derived from the silicon substrate.

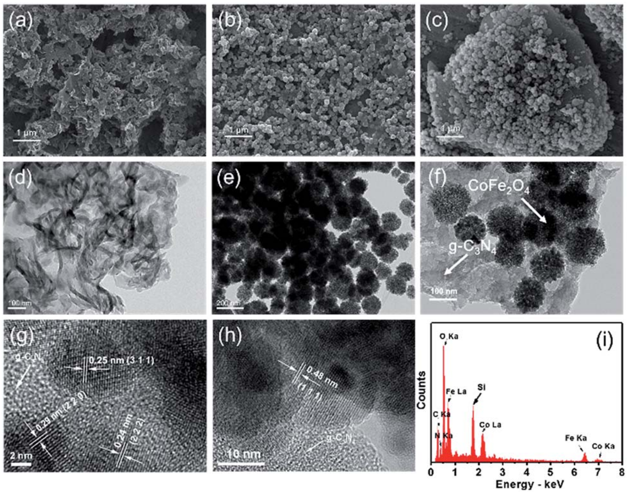

Fig. 1 SEM (a–c) and TEM (d–f) images of (a and d) g-C_3N_4, (b and e) bare $CoFe_2O_4$, (c and f) $CoFe_2O_4$–CNS; (g and h) HRTEM images and (i) EDX pattern of $CoFe_2O_4$–CNS.

The synthesis of the $CoFe_2O_4$ and $CoFe_2O_4$–CNS composites was also confirmed by the XRD and XPS spectra. The $CoFe_2O_4$ showed a typical pattern of spinel ferrite with six well-defined peaks at $2\theta = 18.29°$, 30.08°, 35.44°, 43.06°, 56.97°, and 62.58° (Fig. 2(a)), corresponding to the Bragg planes of (1 1 1), (2 2 0), (3 1 1), (4 0 0), (5 1 1), and (4 4 0), respectively.[38,39] The major crystal phase of $CoFe_2O_4$ was in a good agreement with JCPDS: 22-1086. For the $CoFe_2O_4$–CNS, besides the above six peaks, a characteristic peak at 27.6° corresponding to the (0 0 2) diffraction plane of the CNS was also detected, and no other peaks occurred (Fig. S1†). These results indicate a high purity of the synthesized products. In addition, the XPS survey scan spectra of both materials showed the characteristic peaks of Co, Fe and O, and the extra signal of C (284 eV) and N (400 eV) in the $CoFe_2O_4$–CNS, further confirming the formation of $CoFe_2O_4$ and $CoFe_2O_4$–CNS with high purity (Fig. 2(b)).

The surface properties of the synthesized materials were also evaluated. Despite of the similar ordered mesoporous structure and pore sizes of the two materials (Fig. 3), the $CoFe_2O_4$–CNS had larger specific surface area (89.484 $m^2\ g^{-1}$ *versus* 81.253 $m^2\ g^{-1}$) and larger pore volume (0.163 $cm^3\ g^{-1}$ *versus* 0.108 $cm^3\ g^{-1}$) than $CoFe_2O_4$.

3.2. Catalytic activity for $SO_4^{\bullet-}$ generation and SA degradation

The $CoFe_2O_4$–CNS showed significantly higher activity for PMS activation and SA degradation than the $CoFe_2O_4$ NPs (Fig. 4(a)) and the $CoFe_2O_4$–GO (Fig. S2(a)†). Consistent result was also obtained by the TOC analysis (Fig. 4(b)). In light of the negligible SA removal in the PMS- or catalyst-free controls, this result also implies the critical involvement of $SO_4^{\bullet-}$ in the process. Here, the higher catalytic activity of $CoFe_2O_4$–CNS than $CoFe_2O_4$–GO is likely associated with a better dispersion of the $CoFe_2O_4$ on the CNS with large surface area (Fig. S2(b)†).

The predominant contribution of $SO_4^{\bullet-}$ to the SA degradation in the $CoFe_2O_4$–CNS/PMS system was further confirmed by radicals quenching tests using ethanol or *tert*-butyl alcohol (TBA) as the quencher.[40] Ethanol is commonly used as a scavenger to quickly react with both hydroxyl and sulfate radical species, whereas TBA mainly quenches $OH^{\bullet}$.[41] Our results show that the SA degradation was almost completely inhibited in the presence of excess ethanol (Fig. 5(a)), but was decreased only by 22% (within 5 min) with TBA addition. Therefore, the key role of $SO_4^{\bullet-}$ in the SA degradation can be confirmed.

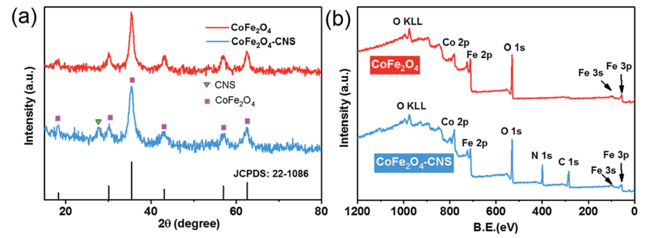

Fig. 2 (a) XRD patterns of $CoFe_2O_4$ and $CoFe_2O_4$–CNS, (b) XPS survey spectra of $CoFe_2O_4$ and $CoFe_2O_4$–CNS.

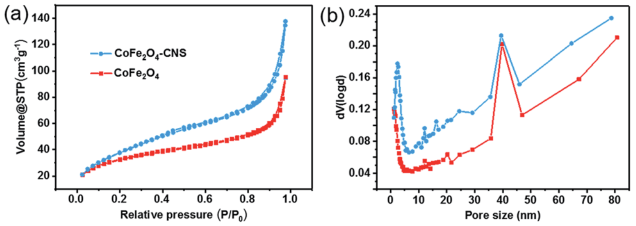

Fig. 3 (a) Nitrogen sorption isotherms and (b) pore size distribution of $CoFe_2O_4$ and $CoFe_2O_4$–CNS.

The SA degradation performances varied under different catalyst dosage, PMS dosage, and the initial pH conditions. The SA removal increased markedly with catalyst dosage from 0.05 to 0.1 g L^{-1}, but increased only slightly when further increasing catalyst dosage to 0.15 g L^{-1} (Fig. 5(b)), indicating that 0.1 g L^{-1} catalyst is sufficient in our reaction system. Increasing PMS concentration also significantly raised the SA removal initially but the removal ratio became relatively stable at high PMS dosage (Fig. 5(c)), likely resulting from self-quenching of the generated $SO_4^{\bullet-}$ by excess PMS.[42] In addition, the catalyst showed stable activity over a wide pH range of 5–10 (Fig. 5(d)). The best performance at initial pH of 10.0 was consistent with previous studies.[43] Here, the significant performance decline at pH 11.0 might be due to a competitive conversion of PMS to less-active dianion (SO_5^{2-}) and $OH^{\bullet}$ under alkaline condition[44] and increased electrostatic compelling between the negatively-charged catalyst and PMS species,[41] whereas the suppression at pH 3.0 should be associated with the deactivation of catalyst with protonation of the surface hydroxyl groups.[3]

$$Co^{2+} + H_2O \rightarrow CoOH^{+} + H^{+} \tag{1}$$

3.3. Magnetic separation and reuse performances

The magnetic properties of the $CoFe_2O_4$ and $CoFe_2O_4$–CNS composites were evaluated, and the magnetic hysteresis loops are shown in Fig. 6. The $CoFe_2O_4$–CNS showed a lower saturation magnetization value (M_s = 56.1 emu g^{-1}) than $CoFe_2O_4$ (M_s = 88.7 emu g^{-1}), which should be due to magnetic property dilution by the nonmagnetic CNS component.

Nevertheless, the $CoFe_2O_4$ was more difficult to be attracted by the magnet, due to smaller sizes of the particles (average size

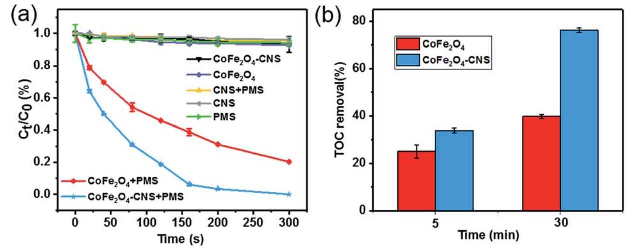

Fig. 4 (a) Removal of SA in different processes. (b) TOC removal of SA at different reaction times. Reaction conditions: [SA] = 10 mg L^{-1}, [PMS] = 0.10 g L^{-1}, [catalyst] = 0.10 g L^{-1}.

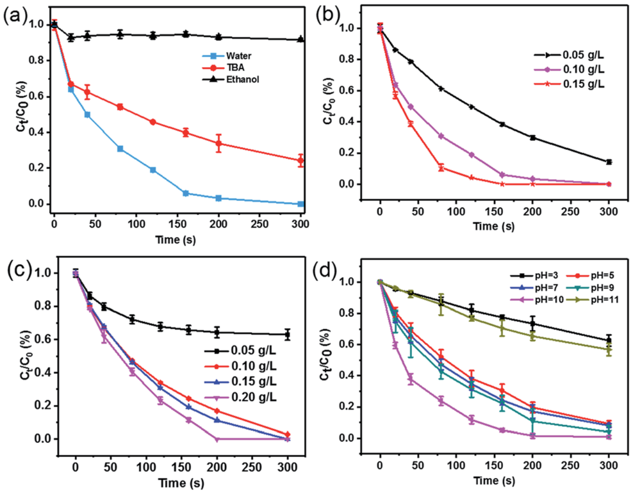

Fig. 5 (a) Effects of radical scavengers on SA degradation in the $CoFe_2O_4$–CNS/PMS system. SA removal efficiencies under different reaction conditions: (b) different catalyst dosage, initial pH = 6.3, [SA] = 10 mg L^{-1}, [PMS] = 0.10 g L^{-1}. (c) Effect of PMS concentration, initial pH = 6.3, [SA] = 10 mg L^{-1}, [catalyst] = 0.10 g L^{-1}. (d) Effect of initial pH, [SA] = 10 mg L^{-1}, [PMS] = 0.10 g L^{-1}, [catalyst] = 0.10 g L^{-1}.

176 nm for $CoFe_2O_4$ *versus* 1.38 μm for $CoFe_2O_4$–CNS) (Fig. S3†). According to the literature,[12,13,45] the smaller nanoparticles are more difficult to recover than larger ones under magnetic field. Therefore, a more effective, rapid magnetical separation of $CoFe_2O_4$–CNS than $CoFe_2O_4$ was achieved in our study (Fig. 6 Inset). Furthermore, for the small-sized $CoFe_2O_4$ particles, an agglomeration would occur during their magnetic separation, and the resulting aggregates are difficult to re-disperse even with intense ultrasonication.[13,46] This explains the much poorer re-suspension of $CoFe_2O_4$ than the larger-sized yet well-dispersed $CoFe_2O_4$–CNS (Fig. 6 Inset).

The $CoFe_2O_4$–CNS also showed good stability during repeated use. After five successive reaction cycles, the system still maintained 94.8% SA removal within 30 min (Fig. S4†). In comparison, the SA removal ratio was 98.6% for the $CoFe_2O_4$ in first cycle and gradually decreased to 69.5% by the fifth cycle (Fig. S4†). The leaching of Co(II) was also more serious in $CoFe_2O_4$ (Fig. S5†). These result indicate a good repeatability and robustness of the $CoFe_2O_4$–CNS far exceeding existing $CoFe_2O_4$ catalysts.

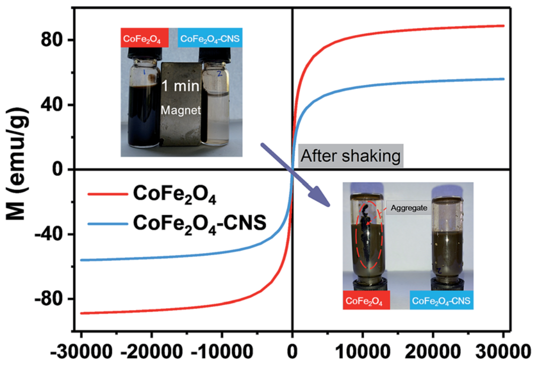

Fig. 6 Magnetic hysteresis loops of $CoFe_2O_4$ and $CoFe_2O_4$–CNS composites at room temperature. Inset: separation and resuspension performance of the synthesized materials.

3.4. Mechanism of PMS activation by $CoFe_2O_4$–CNS

The XPS spectra of $CoFe_2O_4$–CNS and $CoFe_2O_4$ before and after reaction were measured to show the possible changes of the catalysts. The high resolution XPS spectra of the Co 2p3/2 show three peaks at 779.9, 781.2 and 782.8 eV for all the samples (Fig. 7). These peaks were attributed to the Co^{II} in octahedral (B-site Co^{II}) and tetrahedral sites (A-site Co^{II}) and Co^{III} in tetrahedral (B-site Co^{III}), respectively. It is suggested that during the catalysis the B-site Co^{II} would provide electrons to PMS, leading to $SO_4^{\bullet -}$ production and increase of Co^{III} in B-site (eqn (2)). The latter can also accept electrons from PMS to regenerate Co^{II} with concomitant production of SO5$^{\bullet -}$ (eqn (3)), thus maintaining the Co^{II}–Co^{III}–Co^{II} redox cycles for the continuous catalysis.[11,47,48] Our results show that the proportion of B-site Co^{II} in $CoFe_2O_4$–CNS slightly decreased from 58% to 50% after reaction, while B-site Co^{II} in $CoFe_2O_4$ drastically decreased from 63% to 32%. Accordingly, the Co^{III} in tetrahedral of $CoFe_2O_4$–CNS showed less increase (11%) than that of $CoFe_2O_4$ (17%), indicating a more efficient regeneration of B-site Co^{II} in $CoFe_2O_4$–CNS. In addition, the high resolution XPS spectra of Fe 2p (Fig. S6†) showed two major peaks assigned to Fe^{II} (710.6 eV) and Fe^{III} (712.6 eV). The catalytic activity of the Fe^{II}/Fe^{III} redox pair (eqn (4) and (5)) for PMS activation has been demonstrated previously.[11,14,48,49] The $CoFe_2O_4$–CNS showed less decrease in Fe^{II} content than $CoFe_2O_4$ after the reaction. Such an improved Fe^{II} regeneration also contributed to the better sustained activity of $CoFe_2O_4$–CNS in repeated use.

High resolution N 1s spectra (Fig. S7a†) could be fitted into three peaks at 399.1 eV (C–N═C groups, denoted as N1), 399.9 eV (amino groups ((C)$_2$–N–H) connecting with structural defects and incomplete condensation, denoted as N2), 401.2 eV (N–(C)$_3$ in the aromatic ring, denoted as N3). For the $CoFe_2O_4$–CNS, the intensity of N1 peak decreased by 2% after the reaction

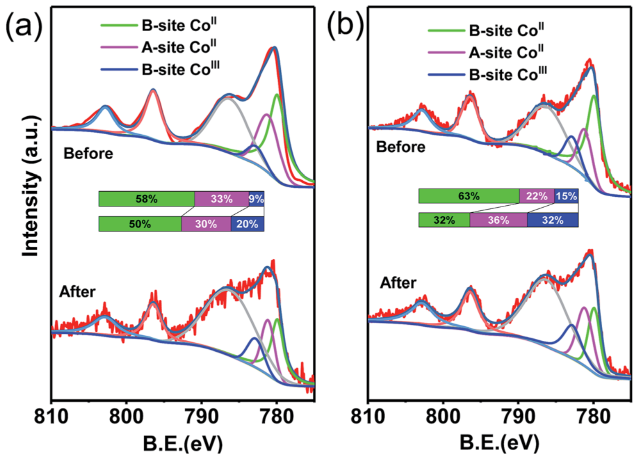

Fig. 7 XPS of Co 2p spectra of (a) $CoFe_2O_4$–CNS composites and (b) $CoFe_2O_4$ before and after the reaction with PMS.

while that of N2 peak increased by 2%. The g-C_3N_4 contains abundant graphitic N corresponding to the sp^2-bonded N that are involved in the triazine rings (N1)[50] and can induce electron transfer from adjacent carbon atoms to nitrogen. Such a feature renders the sp^2 carbon layer of the g-C_3N_4 a high chemical activity.[51–54] Therefore, it is possible that the delocalized electrons from grapheme N on the zigzag edges of CNS might also contributed to the reduction of M^{III} (M = Co or Fe) species, thus the C–N=C groups would be disrupted to form $-NH_2$ or –NH groups (eqn (6) and (7)) (Fig. S7(c)†). This was verified by the FT-IR spectra of $CoFe_2O_4$–CNS which showed increased $-NH_2$ or –NH groups (absorption centred at 3184 cm^{-1})[17] and decreased C–N=C groups after the reaction (Fig. S7(b)†).

$$\equiv Co^{II} + HSO_5^- \rightarrow \equiv Co^{III} + SO_4^{\bullet -} + OH^- \tag{2}$$

$$\equiv Co^{III} + HSO_5^- \rightarrow \equiv Co^{II} + SO_5^{\bullet -} + H^+ \tag{3}$$

$$\equiv Fe^{II} + HSO_5^- \rightarrow \equiv Fe^{III} + SO_4^{\bullet -} + OH^- \tag{4}$$

$$\equiv Fe^{III} + HSO_5^- \rightarrow \equiv Fe^{III} + SO_5^{\bullet -} + H^+ \tag{5}$$

$$\equiv Co^{III} + e_{(C-N=C)}^- \rightarrow \equiv Co^{II} + -NH_2/-NH \tag{6}$$

$$\equiv Fe^{III} + e_{(C-N=C)}^- \rightarrow \equiv Fe^{II} + -NH_2/-NH \tag{7}$$

$$SO_4^{\bullet -} + OH^- \rightarrow SO_4^{2-} + HO^{\bullet} \tag{8}$$

$$SO_4^{\bullet -} + H_2O \rightarrow HSO_4^- + HO^{\bullet} \tag{9}$$

$$SO_4^{\bullet -}/HO^{\bullet} + SA \rightarrow \cdots \rightarrow CO_2 + H_2O \tag{10}$$

In addition, $SO_4^{\bullet -}$ can react with OH^- or water to produce $HO^{\bullet}$ (eqn (8) and (9)). Therefore, the following mechanism of PMS activation by $CoFe_2O_4$–CNS can be proposed (Fig. 8). In the $CoFe_2O_4$ catalyst, the bi-valent metals ($\equiv Co^{II}$ and $\equiv Fe^{II}$) play a centre role in converting PMS into $SO_4^{\bullet -}$, with themselves being oxidized into $\equiv Co^{III}$ and $\equiv Fe^{III}$. The latter can be reduced back to bi-valent metals by PMS, generating less active $SO_5^{\bullet -}$. However, this step is relatively slow, leading to decreased content of $\equiv Co^{II}$ and $\equiv Fe^{II}$ during the catalytic reaction. Here, the introduction of CNS allowed an improved dispersion of the $CoFe_2O_4$ particles, thus more active sites of $\equiv Co^{II}$ and $\equiv Fe^{II}$ could be exposed. In addition, the regeneration of $\equiv Co^{II}$ and $\equiv Fe^{II}$ was reinforced by graphitic N on the zigzag edges of CNS. Such a synergy between $CoFe_2O_4$ and CNS significantly raised the catalytic activity and stability for PMS activation.

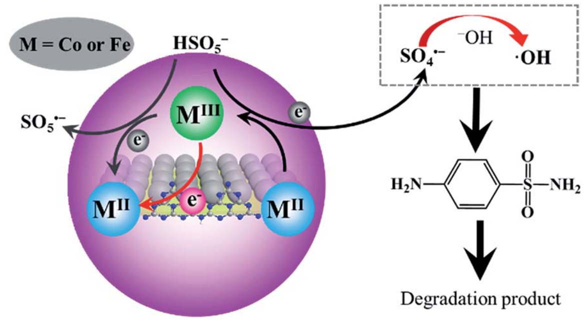

Fig. 8 Mechanisms of PMS activation by $CoFe_2O_4$–CNS for oxidative degradation of SA.

The above results indicate that $CoFe_2O_4$–CNS could be used as an attractive heterogenous catalyst for sustainable pollutant control application, but issues such as Co^{II} leaching and robustness in real environment are still to be addressed in future studies. In addition, the photocatalytic activity of g-C_3N_4 may also be taken advantage of to further strengthen the performance of such $SO_4^{\bullet -}$-based treatment processes.[55,56]

4. Conclusions

A novel $CoFe_2O_4$–CNS nanocomposite was fabricated for PMS activation and SA degradation. It showed obvious advantage over conventional $CoFe_2O_4$ catalyst in terms of catalytic activity, stability, and magnetic separation performance. The superior performance of the $CoFe_2O_4$–CNS was mainly ascribed to a good synergy between the $CoFe_2O_4$ and CNS: the CNS with large specific surface area significantly improved the dispersion of $CoFe_2O_4$ particles, not only enabling the exposure of more active sites to favor PMS activation but also allowing more efficient magnetic separation and resuspension of the material; the CNS also directly contributed to the regeneration of $\equiv Co^{II}$ and $\equiv Fe^{II}$, thereby further improving the catalyst stability during repeated use. This material has the potential for more sustainable water treatment and environmental remediation applications.

Conflicts of interest

There are no conflicts to declare.

Acknowledgements

The authors wish to thank the National Natural Science Foundation of China (51522812, 51538012, 51778597) for the financial support of this work, and thank Dr Zheng Chen at Xi'an Jiaotong-Liverpool University for providing support for the TOC analysis.

References

1 J. Zou, J. Ma, L. Chen, X. Li, Y. Guan, P. Xie and C. Pan, *Environ. Sci. Technol.*, 2013, **47**, 11685–11691.
2 W. D. Oh, Z. Dong, Z. T. Hu and T. T. Lim, *J. Mater. Chem. A*, 2015, **3**, 22208–22217.
3 F. Ghanbari and M. Moradi, *Chem. Eng. J.*, 2017, **310**, 41–62.
4 H. Chen and K. C. Carroll, *Environ. Pollut.*, 2016, **215**, 96–102.
5 J. Wang, Z. Yao, Y. Wang, Q. Xia, H. Chu and Z. Jiang, *Environ. Pollut.*, 2017, **224**, 552–558.
6 G. P. Anipsitakis and D. D. Dionysiou, *Environ. Sci. Technol.*, 2004, **38**, 3705–3712.
7 Y. Fan, W. Ma, J. He and Y. Du, *RSC Adv.*, 2017, **7**, 36193–36200.
8 W. Chu, W. K. Choy and C. Y. Kwan, *J. Agric. Food Chem.*, 2007, **55**, 5708–5713.

9 Q. Yang, H. Choi and D. D. Dionysiou, *Appl. Catal., B*, 2007, **74**, 170–178.

10 W. Zhang, H. L. Tay, S. S. Lim, Y. Wang, Z. Zhong and R. Xu, *Appl. Catal., B*, 2010, **95**, 93–99.

11 Y. Ren, L. Lin, J. Ma, J. Yang, J. Feng and Z. Fan, *Appl. Catal., B*, 2015, **165**, 572–578.

12 L. M. Rossi, N. J. S. Costa, F. P. Silva and R. Wojcieszak, *Green Chem.*, 2014, **16**, 2906–2933.

13 Y. C. Kim, S. Han and S. Hong, *Water Sci. Technol.*, 2011, **64**, 469–476.

14 Y. Yao, Y. Cai, F. Lu, F. Wei, X. Wang and S. Wang, *J. Hazard. Mater.*, 2014, **270**, 61–70.

15 X. Qi, Q. Hu, J. Xu, R. Xie, Y. Jiang, W. Zhong and Y. Du, *RSC Adv.*, 2016, **6**, 11382–11387.

16 B. Buchholcz, H. Haspel, A. Oszko, A. Kukovecz and Z. Konya, *RSC Adv.*, 2017, **7**, 16410–16422.

17 M. Wei, L. Gao, J. Li, J. Fang, W. Cai, X. Li and A. Xu, *J. Hazard. Mater.*, 2016, **316**, 60–68.

18 P. Niu, L. Zhang, G. Liu and H.-M. Cheng, *Adv. Funct. Mater.*, 2012, **22**, 4763–4770.

19 J. Xu, Y. Wang and Y. Zhu, *Langmuir*, 2013, **29**, 10566–10572.

20 J. Xiao, J. Rabeah, J. Yang, Y. Xie, H. Cao and A. Brückner, *ACS Catal.*, 2017, **7**, 6198–6206.

21 H. Zhao, H. Yu, X. Quan, S. Chen, Y. Zhang, H. Zhao and H. Wang, *Appl. Catal., B*, 2014, **152–153**, 46–50.

22 S. Huang, Y. Xu, M. Xie, H. Xu, M. He, J. Xia, L. Huang and H. Li, *Colloids Surf., A*, 2015, **478**, 71–80.

23 Y. Yao, G. Wu, F. Lu, S. Wang, Y. Hu, J. Zhang, W. Huang and F. Wei, *Environ. Sci. Pollut. Res.*, 2016, **23**, 21833–21845.

24 K. L. Corp and C. W. Schlenker, *J. Am. Chem. Soc.*, 2017, **139**, 7904–7912.

25 X. Zhang, X. Xie, H. Wang, J. Zhang, B. Pan and Y. Xie, *J. Am. Chem. Soc.*, 2013, **135**, 18–21.

26 S. G. Dmitrienko, E. V. Kochuk, V. V. Apyari, V. V. Tolmacheva and Y. A. Zolotov, *Anal. Chim. Acta*, 2014, **850**, 6–25.

27 S. Dong, Y. Pi, Q. Li, L. Hu, Y. Li, X. Han, J. Wang and J. Sun, *J. Alloys Compd.*, 2016, **663**, 1–9.

28 W. Zhu, J. Liu, S. Yu, Y. Zhou and X. Yan, *J. Hazard. Mater.*, 2016, **318**, 407–416.

29 A. A. Ahmed, S. Thiele-Bruhn, P. Leinweber and O. Kühn, *Sci. Total Environ.*, 2016, **559**, 347–355.

30 S. T. Khankhasaeva, D. V. Dambueva, E. T. Dashinamzhilova, A. Gil, M. A. Vicente and M. N. Timofeeva, *J. Hazard. Mater.*, 2015, **293**, 21–29.

31 J. Giménez, B. Bayarri, Ó. González, S. Malato, J. Peral and S. Esplugas, *ACS Sustainable Chem. Eng.*, 2015, **3**, 3188–3196.

32 E. Saputra, S. Muhammad, H. Sun, H. M. Ang, M. O. Tade and S. Wang, *Environ. Sci. Technol.*, 2013, **47**, 5882–5887.

33 A. Yan, X. Liu, R. Shi, N. Zhang, R. Yi, Y. Li, G. Gao and G. Qiu, *Solid State Commun.*, 2008, **146**, 483–486.

34 A. Yan, X. Liu, R. Yi, R. Shi, N. Zhang and G. Qiu, *J. Phys. Chem. C*, 2008, **112**, 8558–8563.

35 L. J. Xu, W. Chu and L. Gan, *Chem. Eng. J.*, 2015, **263**, 435–443.

36 T. Li, Y. Lv, J. Su, Y. Wang, Q. Yang, Y. Zhang, J. Zhou, L. Xu, D. Sun and Y. Tang, *Adv. Sci.*, 2017, **4**, 1700226.

37 C. D. Pham, J. Chang, M. A. Zurbuchen and J. P. Chang, *ACS Appl. Mater. Interfaces*, 2017, **9**, 36980–36988.

38 N. Dong, F. He, J. Xin, Q. Wang, Z. Lei and B. Su, *Mater. Res. Bull.*, 2016, **80**, 186–190.

39 N. Dong, M. Zhong, P. Fei, Z. Lei and B. Su, *J. Alloys Compd.*, 2016, **660**, 382–386.

40 G. P. Anipsitakis and D. D. Dionysiou, *Environ. Sci. Technol.*, 2003, **37**, 4790–4797.

41 T. Zhang, H. Zhu and J. P. Croué, *Environ. Sci. Technol.*, 2013, **47**, 2784–2791.

42 H. Liang, H. Sun, A. Patel, P. Shukla, Z. H. Zhu and S. Wang, *Appl. Catal., B*, 2012, **127**, 330–335.

43 Y. Lei, C.-S. Chen, J. Ai, H. Lin, Y.-H. Huang and H. Zhang, *RSC Adv.*, 2016, **6**, 866–871.

44 Y. Feng, J. Liu, D. Wu, Z. Zhou, Y. Deng, T. Zhang and K. Shih, *Chem. Eng. J.*, 2015, **280**, 514–524.

45 G. Friedman and B. Yellen, *Curr. Opin. Colloid Interface Sci.*, 2005, **10**, 158–166.

46 Y. Cai and X. M. Hu, *Desalination*, 2016, **391**, 16–29.

47 X. Li, Z. Wang, B. Zhang, A. I. Rykov, M. A. Ahmed and J. Wang, *Appl. Catal., B*, 2016, **181**, 788–799.

48 Y. Zhao, X. Ma, P. Xu, H. Wang, Y. Liu and A. He, *J. Hazard. Mater.*, 2018, **341**, 228–237.

49 X. J. Yang, X. M. Xu, J. Xu and Y. F. Han, *J. Am. Chem. Soc.*, 2013, **135**, 16058–16061.

50 W. Ho, Z. Zhang, W. Lin, S. Huang, X. Zhang, X. Wang and Y. Huang, *ACS Appl. Mater. Interfaces*, 2015, **7**, 5497–5505.

51 X. Duan, Z. Ao, H. Sun, S. Indrawirawan, Y. Wang, J. Kang, F. Liang, Z. H. Zhu and S. Wang, *ACS Appl. Mater. Interfaces*, 2015, **7**, 4169–4178.

52 X. Duan, Z. Ao, H. Sun, L. Zhou, G. Wang and S. Wang, *Chem. Commun.*, 2015, **51**, 15249–15252.

53 X. Duan, H. Sun, Y. Wang, J. Kang and S. Wang, *ACS Catal.*, 2015, **5**, 553–559.

54 X. Duan, K. O'Donnell, H. Sun, Y. Wang and S. Wang, *Small*, 2015, **11**, 3036–3044.

55 C. Y. Wang, X. Zhang, H. B. Qiu, G. X. Huang and H. Q. Yu, *Appl. Catal., B*, 2017, **205**, 615–623.

56 W. J. Ong, L. L. Tan, Y. H. Ng, S. T. Yong and S. P. Chai, *Chem. Rev.*, 2016, **116**, 7159–7329.